Geometric cohesion in two-dimensional systems composed of star-shaped particles

David Aponte, Nicolas Estrada, Jonathan Barés, Mathieu Renouf, Emilien Azéma

Geometric cohesion in two-dimensional systems composed of star-shaped particles

David Aponte,[1,2,*] Nicolas Estrada,[1,†] Jonathan Barés,[2,‡] Mathieu Renouf,[2,§] and Emilien Azéma[2,3,‖]
[1]*Departamento de Ingeniería Civil y Ambiental, Facultad de Ingeniería, Universidad de los Andes, Bogotá, Colombia*
[2]*LMGC, Université de Montpellier, CNRS, 34090 Montpellier, France*
[3]*Institut Universitaire de France (IUF), 75005 Paris, France*

(Received 29 November 2023; accepted 21 March 2024; published 30 April 2024)

Using a discrete element method, we investigate the phenomenon of geometric cohesion in granular systems composed of star-shaped particles with 3 to 13 arms. This was done by analyzing the stability of columns built with these particles and by studying the microstructure of these columns in terms of density and connectivity. We find that systems composed of star-shaped particles can exhibit geometric cohesion (i.e., a solidlike behavior, in the absence of adhesive forces between the grains), depending on the shape of the particles and the friction between them. This phenomenon is observed up to a given critical size of the system, from which a transition to a metastable behavior takes place. We also have evidence that geometric cohesion is closely linked to the systems' connectivity and especially to the capability of forming interlocked interactions (i.e., multicontact interactions that hinder the relative rotation of the grains). Our results contribute to the understanding of the interesting and potentially useful phenomenon of geometric cohesion. In addition, our work supplements an important set of experimental observations and sheds light on the complex behavior of real, three-dimensional, granular systems.

DOI: 10.1103/PhysRevE.109.044908

I. INTRODUCTION

The mechanical stability of many systems built from granular materials depends essentially on their shear strength. This latter is defined as the maximum shear stress $\tau_{\max}$ that can be applied to the material before it starts flowing. For coarse granular systems, $\tau_{\max}$ is usually predicted using the Coulomb law:

$$\tau_{\max} = c + \sigma \tan \phi, \tag{1}$$

where c is the *cohesion*, σ is the stress normal to the considered plane, and ϕ is the angle of internal friction. The shear strength is thus built from two contributions: cohesive and frictional. In most cohesive granular materials, the cohesion is due to adhesive forces between the grains (e.g., cementation or partial fluid saturation) [1,2], while the frictional contribution results from friction between grains [3–9] and from their shape, more particularly from their angularity [10,11], elongation [11–14], or platyness [15,16].

However, there exist a few granular materials that defy these explanations. One example is materials composed of grains with peculiar shapes, which allow each grain to interlock and/or to mutually entangle. Due to these interactions, these materials exhibit very specific behaviors. One of the most noteworthy aspects of this behavior is that these materials do not flow easily. Instead, they behave as solids, even in the absence of adhesive forces between grains. Because this phenomenon depends strongly on the grain shapes, it is termed *geometric cohesion*, as originally introduced by S. V. Franklin in 2012 [17].

Since the nineties, many studies have focused on understanding granular materials with geometric cohesion. The first works focused on identifying the geometrical features (e.g., the aspect ratio in rodlike particles) inducing solidlike behavior [18–22]. Then, several research groups started studying materials made of particles with nonconvex shapes, such as superballs [23], U-shaped and Z-shaped grains [17,24–27], spiky particles [28–30], and polypods [29–31]. Some of these systems exhibit geometric cohesion, which makes them capable of supporting applied loads and even vibrations [32,33]. Other works have been devoted to the use of geometrical cohesion for architectural purposes [34–37].

Some numerical studies, mainly in two dimensions, have also focused on dense states of nonconvex particle assemblies (U and cross-shaped particles for instance [26,38,39]). Depending on the degree of nonconvexity of the grains, the systems they compose can be hyperstatic or develop long-range correlations over several grain diameters. Some studies (few actually) have focused on flow behavior (e.g., granular systems composed of hexapods in a Couette cell [40]). Finally, two-dimensional experiments have been carried on the packing fraction of systems composed of cross-shaped particles [41]. Together, these works evidence the great potential of this new family of granular materials and highlight the urge to investigate their mechanical properties in a systematic manner [42].

Our main objective was to study the phenomenon of geometric cohesion in granular materials composed of star-shaped particles. Specifically, we aimed to answer the following questions: (i) Do these systems exhibit geometric cohesion? (ii) How does this property depend on the size of

*da.aponte59@uniandes.edu.co, david.aponte@umontpellier.fr
†n.estrada22@uniandes.edu.co
‡jonathan.bares@umontpellier.fr
§mathieu.renouf@umontpellier.fr
‖emilien.azema@umontpellier.fr

the system? (iii) How does this property depend on the specific shape of the particles? and (iv) How does this property depend on the friction between grains?

To tackle these questions, we used numerical simulations in two dimensions using a discrete element method: the contact dynamics (CD) method. We built several samples composed of star-shaped particles with a varying number of arms. These samples were columns of different heights, and each of these columns was subjected to a stability test. We found that systems of star-shaped particles can exhibit geometric cohesion, depending on the geometry of the particles and their frictional properties. We also studied the microstructure of the columns in their initial state, before they get released. We evidence that the emergence of geometric cohesion is closely linked to the system's connectivity, and more particularly to the possibility for particles to interlock (i.e., to restrict their relative rotation).

This article is organized as follows. In Sec. II, we present the geometry of the particles, the numerical method, and the protocol used to build the samples. In Sec. III, we present the results from both the macroscopic and the microstructural viewpoints. Finally, in Sec. IV we summarize our results and present some perspectives for future works.

II. METHODS

A. Simulation of star-shaped particles

The simulations were carried out using the CD method, developed by Dubois and Jean [43,44]. The CD method is a discrete-element method (DEM) based on an implicit time integration of Newton's equations and nonregularized contact laws. In practice, the CD method can be seen as a combination of three main ingredients.

First, the equations of motion for each particle are formulated as differential inclusions in which velocity jumps replace accelerations over a time step Δt. Second, a set of contact laws relate the impulsions exerted at each contact with the change of relative velocity during Δt. The grains are assumed to be perfectly rigid, and the unilateral contact interactions and Coulomb friction law are treated as complementarity relations or set-valued contact laws, involving three physical coefficients: the Coulomb friction coefficient μ, plus two coefficients of restitution (normal and tangential) controlling the amount of energy dissipated during collisions. In all the simulations presented in this paper, the coefficients of restitution were set to zero. Third, forces and velocities are solved simultaneously using a nonlinear (and parallelized [45]) Gauss-Seidel method which consists of solving a single contact problem, with other contact forces being treated as known, and iteratively updating the forces and velocities until a convergence criterion is fulfilled. The iterations in a time step are stopped when the calculated contact forces are stable with respect to the update procedure.

Finally, an implicit time-stepping scheme is used to derive the grains' displacements. A fundamental difference between the CD method and other so-called "smooth" approaches [46] is precisely that no regularization parameters (Hertz-like approach) or dampers are introduced. This makes the CD method unconditionally stable and allows the use of larger time steps than in smooth approaches. This feature is crucial when dealing with very large numbers of grains, especially grains with very nonconvex shapes, which can have a prohibitive number of contacts that can make the systems "very" hyperstatic. A detailed description of the CD method can be found in Refs. [43,44,47] as well as in the Appendices of Ref. [48].

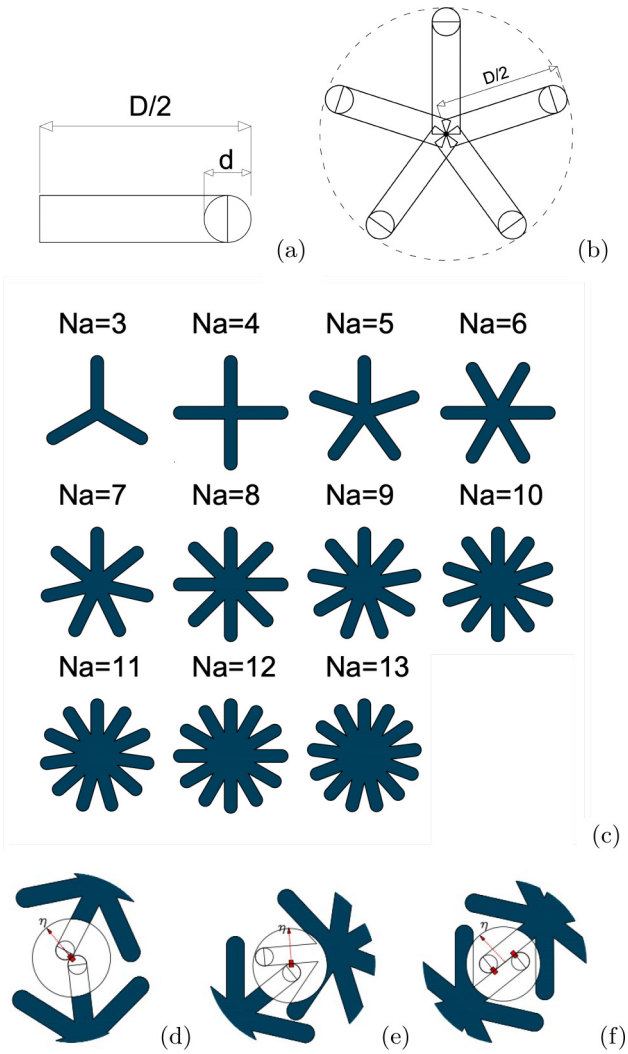

FIG. 1. Particles geometry: (a) Schematic representation of an arm, made from a rectangle and a disk. (b) Schematic representation of a five-arm particle with a diameter (i.e., of the circumscribing circle) D. (c) Star-shaped particles with numbers of arms N_a from 3 to 13. (d) Cap-cap contact (cc) considered as a disk-disk contact. (e) Cap-side contact (cs) considered as a disk-rectangle contact. (f) Side-side contact (ss) considered as two cs-contacts.

Star-shaped particles were constructed by the union of N_a "arms" of thickness d and length $D/2$ distributed in an equiangular manner around the particle's center of gravity, where D is the diameter of the circle circumscribing the particle [see Figs. 1(a) and 1(b)]. One arm was modeled by adding a rectangle of length $L = (D - d)/2$ to a disk of diameter d at its external extremity. In this study, we only considered particles with thin arms and a fixed $D = 9d$. Still, we varied the number of arms, N_a, from 3 to 13. The corresponding family of star-shaped particles is shown in Fig. 1(c).

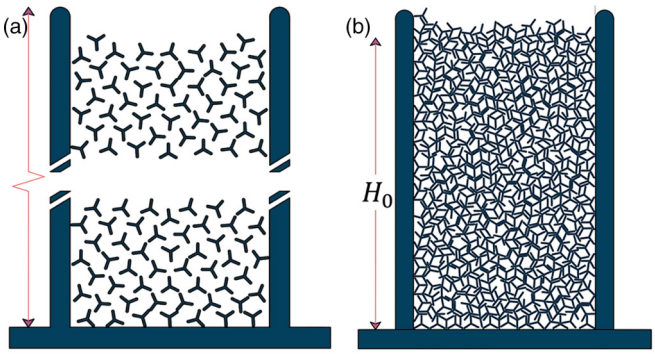

FIG. 2. Sample preparation: (a) Initial state of the sample construction, where N_p randomly oriented particles were initially laid on a triangular lattice (here for particles with three arms). (b) Final state, at the end of the gravity deposition phase; this pile served as an initial state for the stability test.

The interactions between two star-shaped particles can be reduced to a combination of contacts between their arms taken individually. Thus, for contact detection, we used the general scheme shown in Figs. 1(d)–1(f) where the contact between two arms leads to three distinct situations: (i) cap-to-cap *cc*-contacts [Fig. 1(d)], (ii) cap-to-side *cs*-contacts [Fig. 1(e)], and (iii) side-to-side *ss*-contacts [Fig. 1(f)]. In the framework of the CD method, it is common to represent *ss*-contacts as two points of contact. The choice of these points does not affect the resultant force, hence a *ss*-contact can be simply reduced to two *cs*-contacts. The implementation of *ss*-contacts in the framework of the CD method is described in more detail in Ref. [13].

For our simulations, we used the *LMGC90* platform, a multipurpose software developed in LMGC laboratory. It is capable of modeling a collection of deformable or nondeformable particles of many different shapes under various loading conditions.

B. Sample construction and collapse test

All granular columns were prepared following the same protocol. First, for a given set of particles with a number of arms N_a, 4000 randomly oriented particles were initially laid at the nodes of a triangular lattice of edge $1.1D$ inside a rectangular box of width $W_0 = 10D$ [see Fig. 2(a)]. Gravity is then turned on and particles are left free to fall inside the box until the deposit comes to rest [see Fig. 2(b)]. During the deposit, both the local friction coefficient (between grains and with the walls) and the coefficients of restitution were set to zero. The assembly was considered in mechanical equilibrium when a persistent force network was obtained and fluctuations around the mean values of both the solid fraction and the connectivity remained below 0.01%. From this tall column, shorter columns composed of N_p particles were extracted by removing grains from the top. The extracted columns were again balanced by gravity. This protocol was repeated for each value of $N_a \in \{3, ..., 13\}$, in such a way that columns of different initial heights H_0 were built by changing N_p. These two initial steps of the protocol correspond to the preparation of the systems. Then, the friction coefficient μ, between grains and with the walls, was set to 0.5, and the stability of the column was tested. This test consisted on removing the side walls and letting the system evolve under the effect of gravity until it reached a new equilibrium state. The effect of intergranular friction was also tested, varying it between 0.01 and 0.7 for a fixed N_a.

Finally, for the sake of statistical significance, for every configuration, (N_a, N_p), simulations were repeated up to 20 times with independent initial states. Repetitions were stopped once the average and the standard deviation of the most relevant measures were no longer modified by the addition of new simulations. In the end, a total number of 1470 simulations were performed twice: (i) one time for gravity deposition of the particles and (ii) another time for column collapse tests. Note that the activation of friction once the preparation stage is completed is a numerical artifact. It is a way to obtain initially dense arrangements that could have been reached by vibrating the system but in a more time-consuming manner.

III. RESULTS

A. Frictional versus cohesive behavior

In Fig. 3 we show the initial and final states of several columns built with particles with numbers of arms $N_a = 3$ and $N_a = 8$. The initial height ratio, H_0/D, is increased and the induced stability is observed. Two distinct behaviors can be observed. For $N_a = 3$, as classically observed in most stability test problems, the columns collapse into a more or less triangular heap regardless of H_0. In the following, we will refer to this type of response as a *frictional behavior*. In contrast, for $N_a = 8$ the observed response is more complex. For this shape, the integrity of the granular column is maintained, even in the absence of the side walls, for $H_0 < 150D$. In the following, we will refer to this type of response as a *cohesive behavior*. These columns collapse for larger H_0, showing that the behavior becomes frictional as the size of the system increases.

In order to identify which grain shapes induce a frictional or a cohesive behavior, Fig. 4(a) shows the variation of the final scaled height H_f/D (averaged over all repetition for a given value of H_0) as a function of the initial scaled height H_0/D, for all collapse tests and all particle geometries. We note that H_f is defined as the height of the highest particle in the sample after the collapse [see Fig. 4(b)]. Typically, for a frictional behavior $H_f << H_0$ whereas for a cohesive behavior $H_0 \simeq H_f$.

Hence, from Fig. 4(a) we can already identify qualitatively that the star-shaped particles displaying a frictional behavior are those with a number of arms $N_a \in \{3, 4, 5, 13\}$. For these systems, H_f is almost independent of H_0 and remains close to $15D$. Meanwhile, the star-shaped particles displaying a cohesive behavior are those with $N_a \in \{6, ..., 12\}$. In these systems, $H_0 \simeq H_f$ until a "critical" height H_c is reached. H_c can be defined as the height at which H_f stops being approximately equal to H_0 (i.e., the height from which the collapse process starts). It is worth noting that very slender and stable columns can be formed. For example, the column's aspect ratio can be as large as 20 (i.e., the height is equal to 20 times the width of the column) for $N_a = 10$. More interestingly, beyond

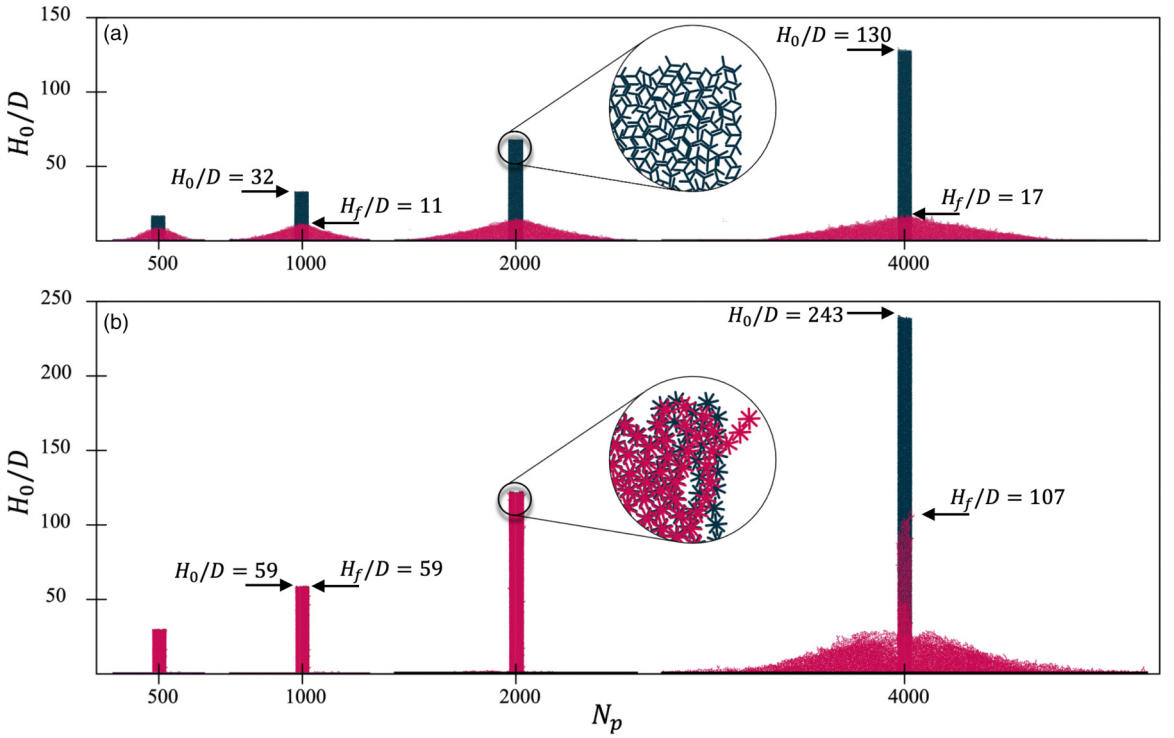

FIG. 3. The initial (dark blue) and final (magenta) states of columns made of star-shaped particles with (a) $N_a = 3$ and (b) $N_a = 8$ are shown, for increasing values of the scaled initial height H_0/D. For $N_a = 3$, the columns collapse towards a more or less triangular heap regardless of H_0. For $N_a = 8$, the integrity of the granular column is maintained, even in the absence of the side walls, for $H_0 < 150D$. Note that both heights are normalized by the diameter of the particles D.

H_c, H_f does not suddenly decline toward $15D$, but a gradual decrease is observed. In other words, we observe a crossover from a purely cohesive to a purely frictional behavior, but this is not a sharp process and metastable cohesive columns persist beyond H_c. Finally, it can be seen that the cohesive behavior depends in a nonmonotonic way on N_a. Indeed, the value H_c from which H_f deviates from H_0 (indicating a partial collapse) first increases from $N_a = 3$ to $N_a = 10$ and then decreases. In the following subsection, a more quantitative description is proposed through the definition of a "collapse ratio" parameter, allowing to continuously describe the crossover from a cohesive to a frictional behavior as H_0 increases.

B. Crossover from cohesive to frictional columns: A measure of column stability

In the previous section, we highlighted that the crossover from a cohesive to a frictional behavior is a smooth transition whose onset is around a critical height, H_c, which depends on the number of arms N_a. In this section, we aim to characterize quantitatively this crossover. For this purpose, let us introduce the collapse ratio r defined in Ref. [32], as a measure of column stability:

$$r = \frac{N_{\text{out}}}{N_p}. \tag{2}$$

As illustrated in Fig. 4(b), N_{out} is the number of particles standing outside the initial column area (in red) while N_p is the total number of particles. For cohesive granular columns, r is expected to be close to zero, while for frictional columns r is significantly higher, close to one. Between these limits, r can be used as an implicit measure of the phenomenon of geometric cohesion by quantifying the level of stability of the cohesive columns.

Figure 5(a) shows the evolution of the collapse ratio r as a function of the initial height H_0/D, for all studied particles. Interestingly, for all columns with a purely frictional behavior (i.e., those with $N_a \in \{3, 4, 5, 13\}$), ratios collapse on a master curve, in which r increases rapidly with H_0 towards a plateau tending asymptotically to 1 for the tallest columns. In contrast, for cohesive columns (i.e., those with $N_a \in \{6, ..., 12\}$), the evolution of r presents two horizontal plateaus. The first, lower, plateau characterizes initially short columns in which $r \to 0$ when $H_0 \to 0$. In this regime, the integrity of the columns is preserved. The second, upper, plateau characterizes tall columns for which $r \to 1$ when $H_0 \to \infty$. In this second regime, columns collapse, exhibiting a frictional behavior. In between, r increases monotonically with an inflection point near $r = 0.5$. Note that, in every case, r slowly tends towards unity without reaching it, since after the collapse a fraction of the particles necessarily remains within the initial column area [see Fig. 4(b)].

Our data are well fitted by the following function introduced by [32]

$$r = \frac{1}{(H_{50}/H_0)^{\alpha} + 1}, \tag{3}$$

where H_{50} is the height for $r = 0.5$ and α is a fitting parameter following a trend similar to that of H_{50}: first, it increases from

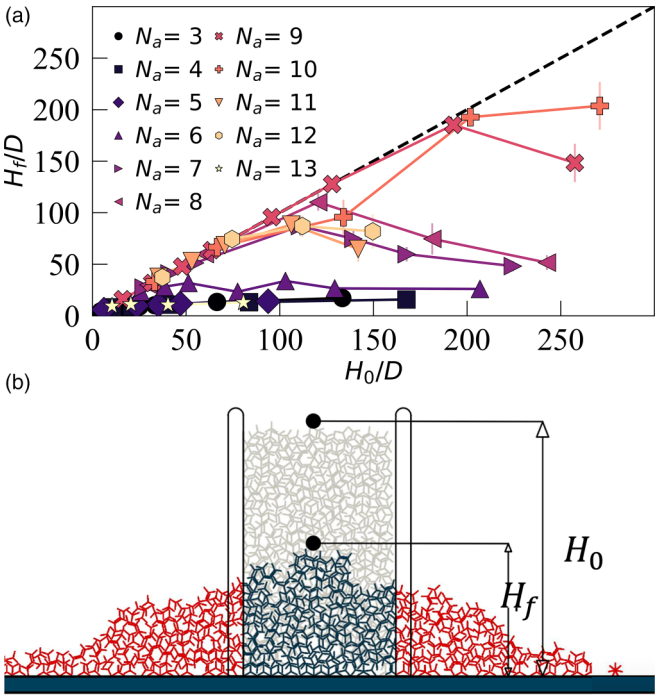

FIG. 4. (a) Scaled final height H_f/D as a function of the normalized initial height H_0/D, for columns composed of grains with different numbers of arms N_a. Error bars represent the standard error between several repetitions for each H_0. (b) Schematic representation of H_0 and H_f. Particles in the initial state are shown in gray color. In the final state, the particles that remain inside the initial area are shown in blue, while that particles that fall outside this area are shown in red.

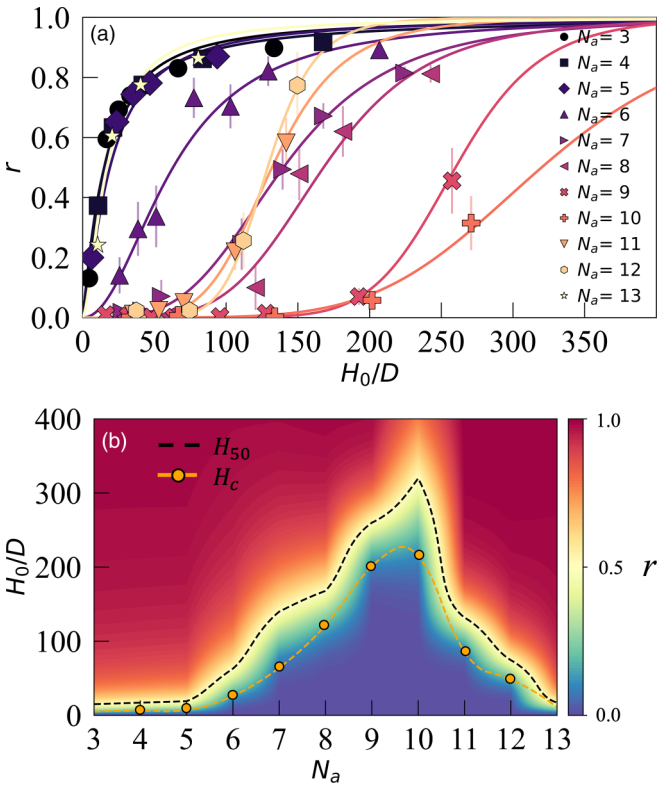

FIG. 5. (a) Evolution of the collapse ratio r of the columns as a function of the scaled initial height H_0/D, for columns composed of star-shaped particles with different numbers of arms N_a. Error bars represent the standard error between several repetitions for each H_0. The lines show a fit of Eq. (3). (b) Stability phase diagram as a function of N_a and the scaled initial height H_0/D. The color scale is proportional to r. The evolution of the critical height H_c and the crossover height H_{50} (see text for a definition) is also shown using dashed lines.

1.2 to 8.7 for $N_a = 10$, and then it decreases to 1.5. H_{50} can be understood as the crossover height from a metastable cohesive behavior to a predominantly frictional behavior, where more than 50% of the particles fall outside of the column. From Eq. (3), we can define H_c in a more accurate way. It corresponds to the height for which $r = 0.1$, which approximates the height where r undergoes a sharp increase. Thus, one gets $H_c = 9^{-1/\alpha} H_{50}$.

Figure 5(b) shows a color map of the collapse ratio, r, as a function of the number of arms N_a. This can be seen as a stability diagram of the granular columns. In this phase diagram, the evolution of the crossover height H_{50} as a function of N_a is plotted with a dashed black line, and the critical height H_c is plotted as a function of N_a in orange. This figure confirms that the stability of cohesive columns increases progressively with N_a and reaches a maximum for $N_a = 10$. Then the stability sharply decreases until the behavior becomes frictional again for $N_a = 13$. Such nonmonotonic behavior reveals complex mechanisms at the microscale when reaching H_c and H_{50}. These mechanisms will be discussed in more detail in Sec. III D.

C. Effect of friction on the stability of geometrically cohesive columns

It is natural to assume that the awakening of geometric cohesion is not only a function of the particle shape but also of the contact friction. To explore this interplay, we first considered columns of particles with $N_a = 6$, for different initial heights H_0. We then vary the value of the interparticle friction $\mu \in \{0.01, 0.3, 0.4, 0.5, 0.6, 0.7\}$. As for the previous data, simulations were repeated several times on initially independent configurations until the mean collapse ratio r and the corresponding standard deviation did not evolve. We carried out up to new 420 simulations.

Figure 6 shows the evolution of the collapse ratio r as a function of H_0/D, for all values of μ. Again, our data are well fitted by Eq. (3) whatever μ. We see that the curves shift progressively from the left to the right as μ is increased. This evidences that both H_c and H_{50} depend on μ. This is shown in the inset of Fig. 6, where both H_c and H_{50} increase to $50D$ and to $100D$, respectively, as μ increases. Note that the parameter α also depends on μ and increases from 1.5 to 3.0. This is most likely because the stability of interlocked interactions increases with μ. The definition and the role of these interactions will be explained in Sec. III D 1. Finally, it is worth noting that geometric cohesion disappears completely when the internal friction tends to zero, at least for the $N_a = 6$ grain shape, where interlocking is impossible.

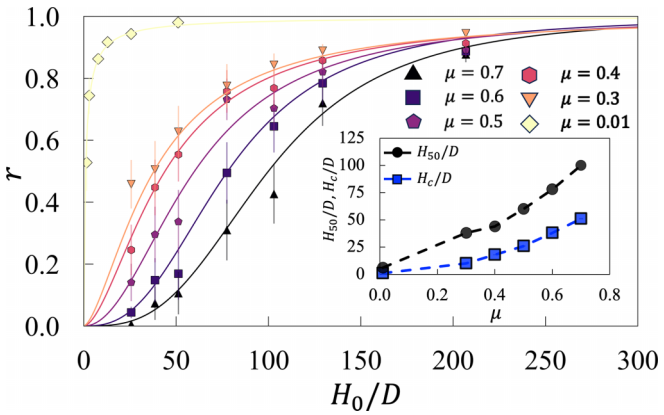

FIG. 6. Collapse ratio r as a function of the scaled initial height H_0/D, for columns composed of grains with $N_a = 6$ arms and for contact friction, μ, from 0.01 to 0.7. Error bars represent the standard error of the collapse ratio. The inset shows the evolution of the critical height H_c/D and the crossover height H_{50}/D as functions of μ.

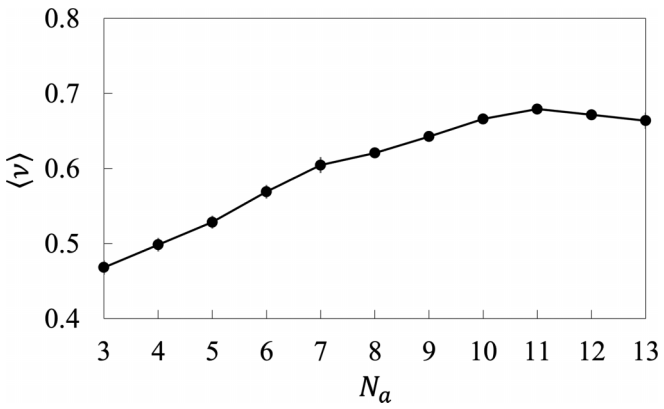

FIG. 7. Averaged packing fraction, $\langle \nu \rangle$, as a function of the number of arms N_a. Data points and bars (too small to be seen) represent the mean and standard error over all repetitions and for all column heights H_0.

D. Microstructure of the initial state

In the previous sections, we described the macroscopic effects of both particle shape and contact friction. To go deeper into the description of these effects, we now explore the microstructure of the systems starting from the study of the initial states of the columns, before the sidewalls are removed, just after the gravity deposition phase. We investigated the geometric organization of the particles in terms of packing fraction and grain connectivity, for different numbers of arms N_a and initial heights H_0. We aim to identify and possibly quantify micro-scale mechanisms that induce the vanishing of the cohesive response, explaining the crossover from a cohesive to a frictional behavior.

1. Packing fraction and grain connectivity

The first and most natural approach when dealing with the resistance of granular materials is to study their density and its relationship with strength. The packing fraction is a measure of how dense the material is. It is calculated as

$$\nu = \frac{V_p}{V}, \tag{4}$$

where V_p is the volume occupied by the particles and V is the total volume.

Figure 7 shows the evolution of the average packing fraction, $\langle \nu \rangle$, as a function of the number of arms, N_a. It should be noted that, for a fixed value of N_a, the average runs over all initial heights H_0. As a general observation, $\langle \nu \rangle$ increases with N_a, reaches a maximum for $N_a = 11$, and then remains at high values until $N_a = 13$. Moreover (although not shown here), we verified that packing fraction profiles [i.e., $\nu(y/D)$] are almost constant within the bulk; thus, ν fails to explain the emergence and disappearance of geometric cohesion. Similarly, Table I presents the global packing fraction $\langle \nu \rangle$ for the largest systems analyzed. It should be noted that the height H_0/D of all systems depends on N_a. As it will be shown in the following paragraphs, a clearer link between microstructure and geometric cohesion can be established by analyzing the systems' connectivity.

Along with the packing fraction, the "compactness" of the initial states can also be analyzed in terms of the connectivity of the particles. More precisely, the main effect of shape nonconvexity is to allow several types of contacts between the particles as illustrated in Fig. 8 for $N_a = 8$. In this case, up to four contacts can be formed between two star-shaped particles. These contacts can be point-contacts (i.e., a combination of *cc* and/or *cs* contacts) or a mix between point-contacts and linear contacts, with two *cs* and one *ss* contact. Note that, since *ss* contacts represent two geometrical constraints, they should be counted twice when enumerating contacts. In the following, we will refer to "simple" (i1), "double" (i2), "triple" (i3), and "quadruple" (i4) interactions when particles interact through, one, two, three, and four contacts, respectively. Note that although we used a particle with eight arms as an example, the same types of interactions occur between star-shaped particles with different numbers of arms.

Then, we can identify several ways of computing the coordination number. First, it can be defined as the mean number of neighbors per particle (i.e., multiple contacts are only seen

TABLE I. Global packing fraction $\langle \nu \rangle$ and maximum average initial height H_0/D for the largest systems analyzed. The number of arms N_a and the number of particles N_p are also presented.

N_a	N_p	H_0/D	$\langle \nu \rangle$
3	4000	133.4	0.47
4	4000	167.6	0.49
5	2000	93.7	0.52
6	4000	206.8	0.56
7	4000	224.4	0.60
8	4000	242.5	0.62
9	4000	257.5	0.64
10	4000	270.8	0.66
11	2000	141.8	0.67
12	2000	149.6	0.67
13	1000	80.5	0.66

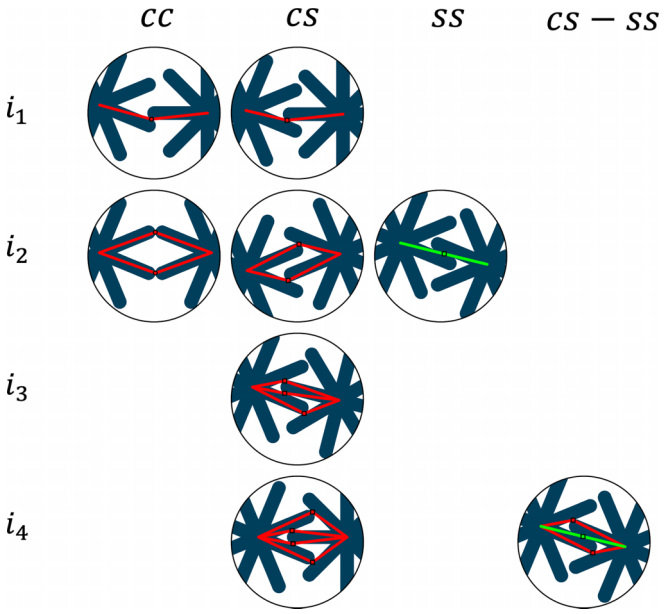

FIG. 8. Schematic representation of the types of contacts that can be observed between the strongly nonconvex grains explored in this study. Without any loss of generality, here examples are given for particles with $N_a = 8$ arms. Red lines represent *cc* or *cs* contacts, and green lines represent *ss* contacts (counted twice since a *ss* contact represents two geometrical constraints).

as one interaction). In this case, we call it Z. Then, it can be defined as the connectivity number, Z_c, which is the mean number of contacts per particle. Note that, for the ideal case of circular particles (i.e., for $N_a \to \infty$) $Z = Z_c$.

Figure 9(a) shows Z and Z_c, as functions of the number of arms N_a. It can be seen that Z is almost constant with N_a. This means that the number of neighboring particles is similar in all samples and independent of N_a. On the contrary, Z_c increases from $\simeq 6$ to $\simeq 10$ when N_a goes from 3 to 10, and then decreases to $\simeq 7$ for $N_a = 13$. This is surprising since a $Z_c \simeq 6$ is expected for every shape because the initial packings were built with frictionless particles [49,50]. Indeed, frictionless noncircular particles are characterized by 3 degrees of freedom (two translations and one rotation) so that the isostatic condition implies $Z_c = 6$. This means that assemblies of star-shaped particles are hyperstatic, and the degree of hyperstaticity of the columns at the initial state varies nonmonotonically with N_a. We note that the hyperstatic character of assemblies of nonconvex grains has been already reported for highly nonconvex shapes, more precisely for U-shaped and star-shaped particles in 2D [26,39]. Interestingly, the maximum in Z_c occurs at $N_a = 10$, which also corresponds to the most stable (i.e., geometrically cohesive) columns (see Sec. III B). Nevertheless, we notice that a high degree of hyperstaticity is not a sufficient condition to obtain geometric cohesion. For instance, the columns with $N_a = 4$, 5, and 13 are hyperstatic but they exhibit a frictional behavior.

For further insight, in Fig. 9(b) we plot the evolution of the partial connectivity numbers, Z_{i1} to Z_{i4}, as functions of the number of arms N_a, such that $Z_c = Z_{i1} + Z_{i2} + Z_{i3} + Z_{i4}$. We see that Z_{i1} and Z_{i2} decrease with N_a, while Z_{i3} increases. More interestingly, Z_{i4} presents a peak value for $N_a = 10$. As

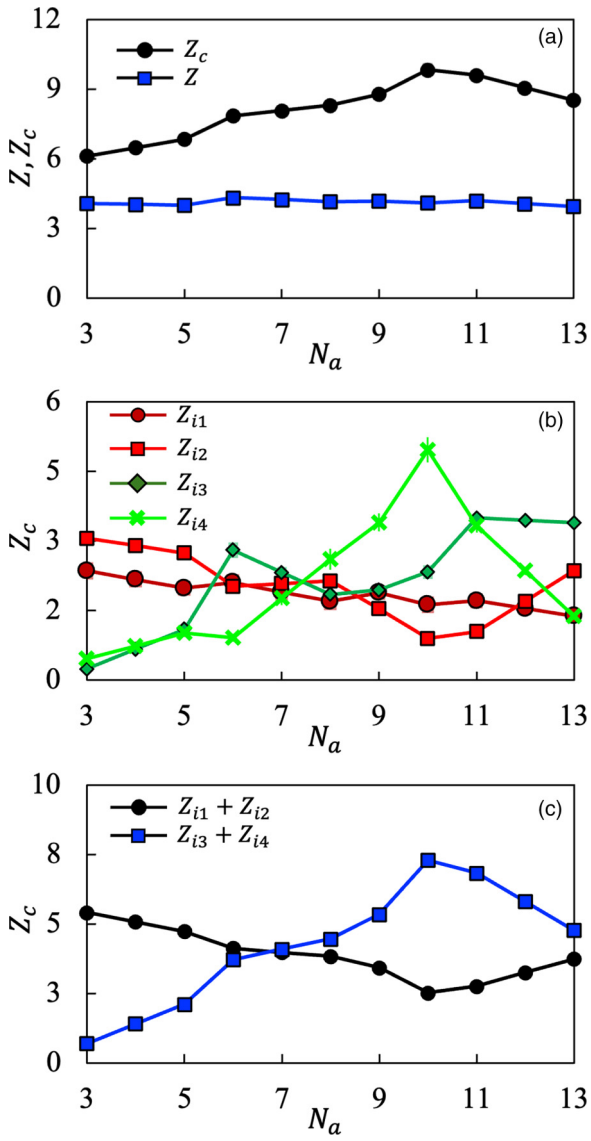

FIG. 9. (a) Coordination number Z and connectivity number Z_c as functions of the number of arms N_a. (b) Evolution of the partial connectivity numbers Z_{i1} (dark red circle), Z_{i2} (clear red square), Z_{i3} (dark green lozenge), Z_{i4} (clear green cross) as functions of N_a. (c) The connectivity numbers distinguishing $Z_{i1} + Z_{i2}$ and $Z_{i3} + Z_{i4}$. The bars represent the standard error of the plotted data.

highlighted before, this value of N_a corresponds to the most cohesive columns. Thus, the increase in Z_c is explained by the gain in local interactions with more than 3 contacts up to $N_a = 10$. Beyond, the decrease in Z_c is explained by the loss of these highly connected local interactions.

More fundamentally, Z_{i3} and Z_{i4} quantify locally interlocked and closely packed structures preventing, or at least restricting, the relative rotation of the grains. With this in mind, in Fig. 9(c) we distinguish the total contribution of $i1$ and $i2$ interactions ($Z_{i1} + Z_{i2}$) from that of $i3$ and $i4$ ($Z_{i3} + Z_{i4}$). Remarkably, for shapes that only exhibit a frictional behavior (i.e., for $N_a \in \{3, 4, 5, 13\}$) simple and double interactions dominate, meaning that: $Z_{i1} + Z_{i2} > Z_{i3} + Z_{i4}$. On the contrary, for shapes that exhibit a cohesive behavior

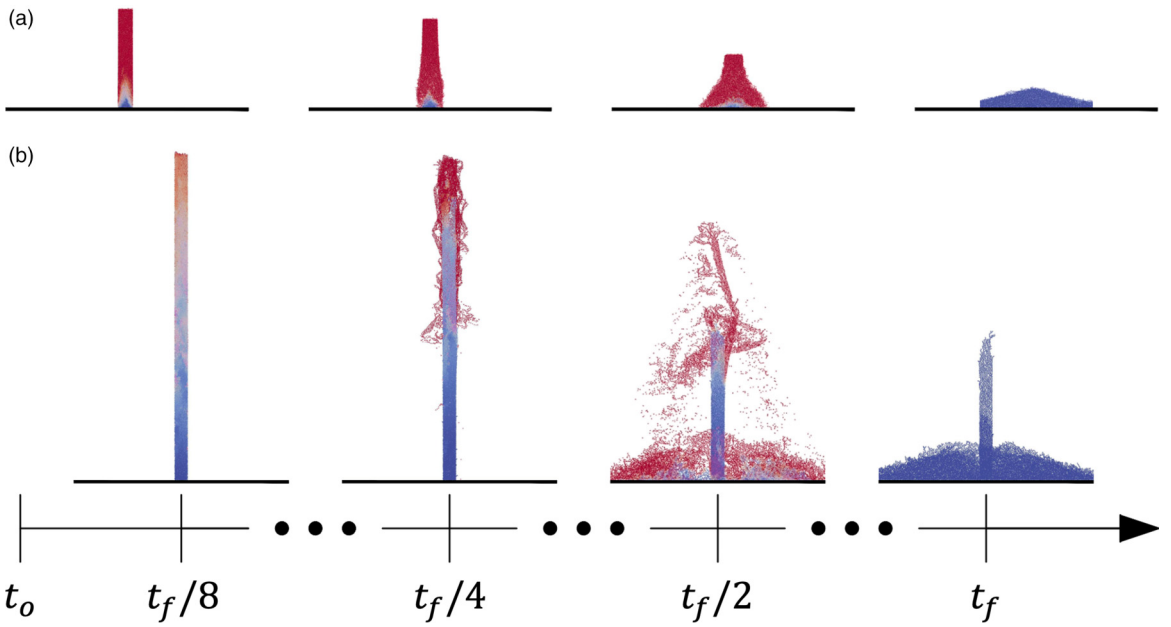

FIG. 10. Collapse sequence for a column with (a) $N_a = 3$ arms and an initial height $H_0/D = 66$ and (b) for $N_a = 8$ and $H_0/D = 240$. t_f corresponds to the final time from which the heap is at rest. The color scale represents the particles' velocity.

(i.e., for $N_a \in \{6...12\}$), complex, multicontact, and thus potentially interlocked interactions are dominant.

Thus, it can be assumed that geometric cohesion is a complex phenomenon requiring the interplay of at least three conditions: (i) hyperstaticity, (ii) interlocking interactions avoiding grain rotation in "sufficient" proportions, and (iii) a sufficiently large local friction coefficient.

2. *Collapse sequence and connectivity profiles*

To reinforce the hypothesis formulated above, in this section, we focus more specifically on the collapse mechanism and how observables evolve in the system around H_c and eventually display a crossover.

In particular, we analyzed the evolution of the connectivity as a function of the height, $Z_c(y)$, in a given column before removing the sidewalls. We expect this quantity to vary as y increases so that at least one of the conditions formulated above is lost. For the sake of clarity, in the following, we will focus only on the columns composed of particles with $N_a = 3$ (frictional behavior) and with $N_a = 8$ (cohesive behavior). In both cases, the friction coefficient is fixed to $\mu = 0.5$.

Figure 10 shows the collapse sequence of two different columns: (a) for $N_a = 3$ arms and an initial height of $H_0/D = 66$ and (b) for $N_a = 8$ and $H_0/D = 240$. For this latter case, we consider a cohesive metastable column with $H_0 > H_c$. The color scale is proportional to the particles' velocity. Basically, for the frictional column, the system forms an initial barrel which then spreads laterally. On the contrary, for the metastable cohesive column, the particles start to fall from the top, while the bottom remains relatively stable. This suggests that particles are better connected at the bottom of the column than at the top, preventing a generalized collapse.

Figure 11 shows the connectivity profiles $Z_c(y)$ (left side) and the partial connectivity number (right side) at the initial

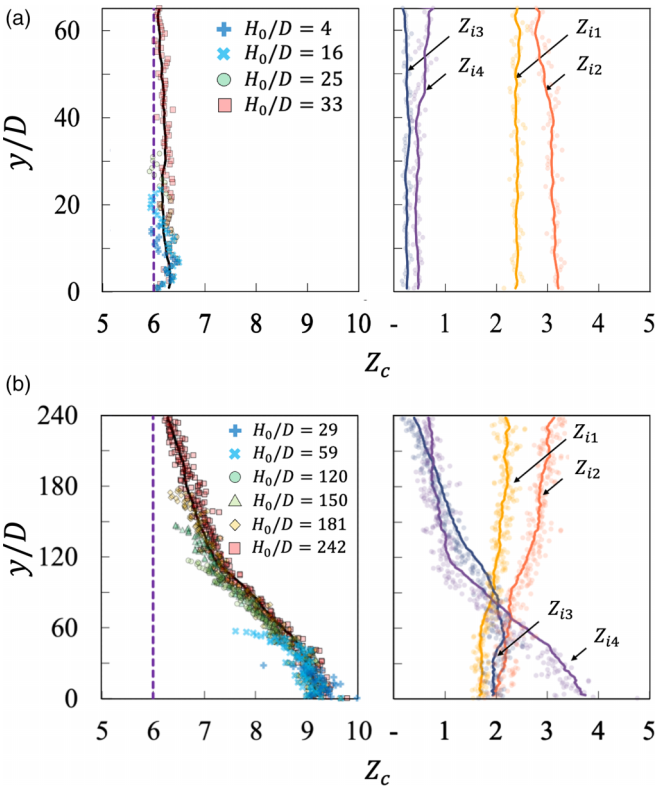

FIG. 11. Connectivity profiles $Z_c(y)$ as functions of the vertical position y, scaled by the diameter D, for columns with (a) $N_a = 3$ arms and (b) $N_a = 8$. On the left side of the figure, the average of Z_c is shown using a full line, and the limit z_{iso} is shown using a purple dashed line. On the right-hand side, we show the partial connectivity number profiles Z_{i1} to Z_{i4} as functions of y/D; the data for all initial heights H_0 are shown using the same color for the sake of clarity.

state, as functions of the vertical position, y, scaled by the particle diameter D, for columns composed of particles with (a) $N_a = 3$ arms and (b) $N_a = 8$, and for various values of the initial height H_0. For a given H_0, the profiles are averaged over several independent initial states. For columns with $N_a = 3$, $Z_c(y)$ is approximately constant and close to the expected isostatic value of $Z_c \simeq 6$. On the contrary, for columns exhibiting a cohesive behavior (here for $N_a = 8$) $Z_c(y)$ significantly evolves with y/D. More precisely, for $H_0/D \leqslant 59$, $Z_c(y)$ values are very high, close to 8 or 9. These columns exhibit a solidlike behavior (see also Fig. 3). For larger values of H_0/D, $Z_c(y)$ progressively declines towards 6 as y/D increases. It is interesting to note that, for all y/D, $Z_c(y)$ nearly coincides whatever the initial height of the columns. This finding results from the column construction protocol presented in Sec. II B. More specifically, for $N_a = 8$, $Z_c(y)$ is close to 9 in the first layers of the column, and then it decreases almost linearly to $\simeq 7$, as y/D increases from 30 to 90. It then continues to decrease less rapidly beyond $y/D \sim 90$, tending towards the expected isostatic value of $Z_c \simeq 6$ for the highest altitudes. In other words, the transition from a metastable to a frictional behavior is correlated with a change from a hyperstatic to an isostatic nature of the contact network as y/D increases. This is consistent with the collapse mechanism of the cohesive columns starting at the top (i.e., for the largest values of H_0).

A deeper insight can be achieved by analyzing the partial connectivity profiles Z_{i1}, Z_{i2}, Z_{i3}, and Z_{i4}, as presented on the right-hand side of Fig. 11 for (a) $N_a = 3$ and (b) $N_a = 8$. For $N_a = 3$, all the profiles remain nearly constant, regardless of the initial height H_0/D. In particular, $Z_{i1} + Z_{i2} > Z_{i3} + Z_{i4}$. In contrast, for $N_a = 8$, $Z_{i3} + Z_{i4}$ is higher than $Z_{i1} + Z_{i2}$ in the first layers. A crossover is observed around $y/D \simeq 70$. Near this point, cohesive columns transform into metastable ones. This is also explained by the decrease of $Z_c(y)$ in this range of heights. Finally, Z_{i3} and Z_{i4} vanish with y, while Z_{i1} and Z_{i2} remain nearly constant and close to three. Note that interactions with three or four contacts correspond to the maximal possible connectivity between star-shaped particles, as it was shown in Fig. 8. Thus, it is indeed the loss of local interlocked structures with three or more contacts that induces a progressive destabilization of cohesive columns. This leads to their collapse for the highest values of H_0.

3. Improving the stability of geometrically cohesive columns

The connectivity profiles shown in the previous subsection are the result of the sample preparation method presented in Sec. II B. The gravitational deposition method is somehow biased by the fact that the velocity acquired by the particles when deposited depends on their initial height. As a result, grains at higher altitudes experience greater dynamic states than those at the base of the column. At the same time, particles at the top part of the columns are less subjected to the weight of the upper layers and therefore require fewer contacts to be stabilized. So, to further strengthen the hypothesis of the necessary role of local interlocked structures with three or more contacts to obtain geometric cohesion, we conducted the following test. We considered all the initial states previously constructed for $N_a = 8$ and $H_0/D \in \{117, 145, 175, 240\}$. Then, these columns were compressed vertically by imposing a constant stress on the top wall, while maintaining the side walls position and zero friction between the particles. The imposed force to compress the columns was approximately equal to the weight of the column. The compression was stopped as soon as mechanical equilibrium was reached (i.e., when a persistent contact force network was obtained). Note that as explained in Sec. II particles are rigid. Regarding the solid fraction, for the shortest column $\langle \nu \rangle$ increased from 0.65 to 0.66, and for the tallest column $\langle \nu \rangle$ increased from 0.64 to 0.65. Once stabilized, a collapse test was carried out as described in Sec. II B, by setting the contact friction to 0.5 and removing the side walls. This represented a total of 85 simulations.

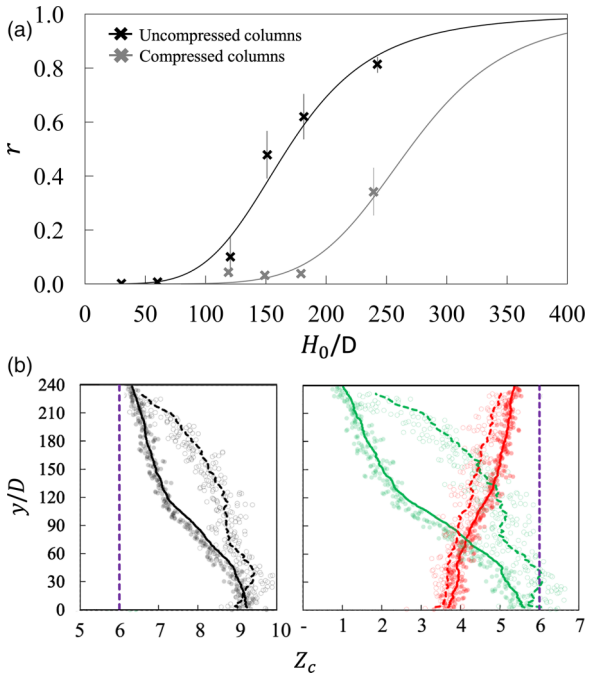

FIG. 12. (a) Evolution of the collapse ratio r for $N_a = 8$ arms, for both uncompressed and compressed columns. Error bars represent the standard error. (b) Profiles of the connectivity number $Z_c(y)$ (black) and partial connectivity numbers $Z_{i1} + Z_{i2}$ (red) and $Z_{i3} + Z_{i4}$ (green), as functions of the vertical position y/D for initially uncompressed (full lines) and compressed (dashed lines) columns with $H_0/D = 240$.

Figure 12(a) shows the evolution of the collapse ratio r as a function of the scaled initial height H_0/D for $N_a = 8$ arms (same as in Fig. 5), together with the four points corresponding to the mechanically compressed columns. We see that the first three metastable cohesive columns (i.e., $H_0 \in \{117, 145, 175\}D$) become now fully cohesive. Similarly, the column that initially exhibited a frictional behavior (i.e., $H_0 = 240D$) now exhibits a metastable cohesive behavior, with r changing from 0.9 to 0.4. This result, although remarkable, is not completely new and has been observed by other authors, comparing experimentally the stability of columns of nonconvex grains initially compacted by vibration [32,33]. Figure 12(b) shows the evolution of the connectivity profile $Z_c(y)$ of the two averaged initial states, i.e., for uncompressed

(plain lines, full symbols) and compressed (dashed lines, empty symbols) columns for $H_0/D = 240$. We see that, in the compressed columns, the connectivity profile remains roughly constant around 9 up to an altitude of $y/D \sim 150$. This evidences a higher connectivity than that of uncompressed columns. Similarly, the crossover observed in the evolution of partial connectivity occurs at a higher altitude for the compressed columns.

IV. SUMMARY AND DISCUSSION

In summary, using contact dynamics simulations, we investigated the phenomenon of geometric cohesion in granular systems composed of star-shaped particles. To do so, we built several samples composed of particles with a varying number of arms. We built columns of different heights that were subjected to a stability test. We aimed at answering the following questions: (i) Do these systems exhibit geometric cohesion? (ii) How does this property depend on the size of the system? (iii) How does this property depend on the shape of the particles? (iv) How does this property depend on the friction between the grains? In the following paragraphs, we present our main conclusions.

First, we found that some of the granular systems investigated do exhibit geometric cohesion. This property is closely linked to the shape of the particles, and in our case to the number of arms of these particles. Specifically, we did not observe geometric cohesion for particles with 3, 4, 5, and 13 arms. In contrast, we observed geometric cohesion for particles with 6 to 12 arms. For the set of shapes explored here, the cohesive response is maximized for particles with 10 arms, and the columns can behave in a solidlike manner up to heights as large as 20 times the width of the column. This is consistent with experimental observations for rodlike particles [18–22], staples [17,24,25], Z-shaped particles [27], and hexapods [32,33,38]. We also show that these systems behave as solids up to a certain critical height. From this point, following gradual crossover, the systems transition from a cohesive behavior to a frictional one.

Second, we see that geometric cohesion cannot be fully attributed to the geometry of the particles; in fact, friction between the particles also plays a crucial role. We found that geometric cohesion, quantified in terms of the critical height at which the crossover starts, strongly increases with the local friction. This is to be expected, since friction enhances the stability of local interactions, thus reinforcing the global stability of the column. The importance of the local friction has also been shown experimentally, by comparing the response of polypods composed of different materials with different friction coefficients [33].

Third, we studied the microstructure of the columns in their initial state, in terms of packing density and connectivity. We found that geometrically cohesive columns tend to be denser than frictional columns, but this correlation is not sufficient to explain or predict the emergence of solidlike behavior. We found that the microstructural feature that is the most useful to explain and predict geometrical cohesion is the particles' connectivity. In particular, geometrically cohesive granular systems tend to be hyperstatic and are characterized by a large proportion of interlocked interactions between grains. In these interactions, the relative rotation between particles is hindered by being composed of three or four contacts. We hypothesize that, without the possibility of forming interlocked or entangled interactions, geometric cohesion cannot occur.

We emphasize that geometric cohesion in granular matter is a physically interesting phenomenon, but also a potentially useful one for engineering purposes. Important examples are granular structures made to protect coastlines or riverbanks against erosion, or more generally free-standing structures that can be disassembled easily and undergo strong external loading. This could be a way of making strong constructions while decreasing their carbon footprint. Even if the results obtained in this study are only valid for two-dimensional systems, they constitute an exploration and a description of a microstructure that must stay valid in real systems. In other words, the study allowed us to identify the physical origin of these types of complex phenomena, which remain true whatever the system dimension. We are currently extending our work to three-dimensional systems, using both experiments and simulations, and we plan to present our results in future publications. Additionally, it must be noted that the simulations presented in this article were carried out for one thickness of the arms and one width of the system; thus, it would be important to verify these results in a more general framework.

ACKNOWLEDGMENTS

This project is supported by the LabEx NUMEV within the I-Site MUSE (ANR 2011-LABX-076). We also acknowledge the support of the High-Performance Computing Platform MESO@LR. Finally, we warmly thank Jaime José Castro and Jaime Wills for their valuable contributions and stimulating discussions during the initial stages of this work.

[1] J. K. Mitchell and K. Soga, *Fundamentals of Soil Behavior* (John Wiley & Sons, New York, NY, 2005).

[2] B. Das, *Advanced Soil Mechanics* (CRC Press, Boca Raton, FL, 2006).

[3] P. W. Rowe and G. I. Taylor, Proc. R. Soc. London A **269**, 500 (1962).

[4] M. R. Horne and J. F. Baker, Proc. R. Soc. London A **286**, 79 (1965).

[5] A. E. Skinner, Géotechnique **19**, 150 (1969).

[6] L. Oger, S. Savage, D. Corriveau, and M. Sayed, Mech. Mater. **27**, 189 (1998).

[7] A. Taboada, K.-J. Chang, F. Radjaï, and F. Bouchette, J. Geophys. Res.: Solid Earth **110**, 2003JB002955 (2005).

[8] A. Taboada, N. Estrada, and F. Radjaï, Phys. Rev. Lett. **97**, 098302 (2006).

[9] N. Estrada, A. Taboada, and F. Radjaï, Phys. Rev. E **78**, 021301 (2008).

[10] E. Azéma, F. Radjai, and G. Saussine, Mech. Mater. **41**, 729 (2009).
[11] CEGEO, B. Saint-Cyr, K. Szarf, C. Voivret, E. Azéma, V. Richefeu, J.-Y. Delenne, G. Combe, C. Nouguier-Lehon, P. Villard *et al.*, Europhys. Lett. **98**, 44008 (2012).
[12] E. Azéma and F. Radjaï, Phys. Rev. E **81**, 051304 (2010).
[13] E. Azéma, F. Radjai, and F. Dubois, Phys. Rev. E **87**, 062203 (2013).
[14] E. Azéma, I. Preechawuttipong, and F. Radjai, Phys. Rev. E **94**, 042901 (2016).
[15] M. Boton, E. Azéma, N. Estrada, F. Radjaï, and A. Lizcano, Phys. Rev. E **87**, 032206 (2013).
[16] M. Boton, N. Estrada, E. Azéma, and F. Radjaï, Eur. Phys. J. E **37**, 116 (2014).
[17] S. V. Franklin, Phys. Today **65**(9), 70 (2012).
[18] A. P. Philipse, Langmuir **12**, 1127 (1996).
[19] K. Stokely, A. Diacou, and S. V. Franklin, Phys. Rev. E **67**, 051302 (2003).
[20] J. Blouwolff and S. Fraden, Europhys. Lett. **76**, 1095 (2006).
[21] K. Desmond and S. V. Franklin, Phys. Rev. E **73**, 031306 (2006).
[22] M. Trepanier and S. V. Franklin, Phys. Rev. E **82**, 011308 (2010).
[23] Y. Jiao, F. H. Stillinger, and S. Torquato, Phys. Rev. E **79**, 041309 (2009).
[24] N. Gravish, S. V. Franklin, D. L. Hu, and D. I. Goldman, Phys. Rev. Lett. **108**, 208001 (2012).
[25] S. V. Franklin, Europhys. Lett. **106**, 58004 (2014).
[26] T. A. Marschall, S. V. Franklin, and S. Teitel, Granular Matter **17**, 121 (2015).
[27] K. A. Murphy, N. Reiser, D. Choksy, C. E. Singer, and H. M. Jaeger, Granular Matter **18**, 26 (2016).
[28] I. Malinouskaya, V. V. Mourzenko, J.-F. Thovert, and P. M. Adler, Phys. Rev. E **80**, 011304 (2009).
[29] J. de Graaf, R. van Roij, and M. Dijkstra, Phys. Rev. Lett. **107**, 155501 (2011).
[30] A. G. Athanassiadis, M. Z. Miskin, P. Kaplan, N. Rodenberg, S. H. Lee, J. Merritt, E. Brown, J. Amend, H. Lipson, and H. M. Jaeger, Soft Matter **10**, 48 (2014).
[31] F. Ludewig and N. Vandewalle, Phys. Rev. E **85**, 051307 (2012).
[32] J. Barés, Y. Zhao, M. Renouf, K. Dierichs, and R. Behringe, EPJ Web Conf. **140**, 06021 (2017).
[33] Y. Zhao, J. Ding, J. Barés, H. Zheng, K. Dierichs, A. Menges, and R. Behringer, EPJ Web Conf. **140**, 06011 (2017).
[34] G. Borden and M. Meredith, in *Matter: Material Processes in Architectural Production* (Routledge, Oxford, UK, 2011).
[35] K. Dierichs and A. Menges, Archit. Des. **82**, 74 (2012).
[36] P. Aejmelaeus-Lindström, J. Willmann, S. Tibbits, F. Gramazio, and M. Kohler, Granular Matter **18**, 28 (2016).
[37] K. Dierichs and A. Menges, Archit. Des. **87**, 88 (2017).
[38] H. Zheng, D. Wang, J. Barés, and R. Behringer, EPJ Web Conf. **140**, 06014 (2017).
[39] T. A. Marschall and S. Teitel, Granular Matter **22**, 4 (2020).
[40] M. Mohammadi, D. Puzyrev, T. Trittel, and R. Stannarius, Phys. Rev. E **106**, L052901 (2022).
[41] R. Stannarius and J. Schulze, Granular Matter **24**, 25 (2022).
[42] D. Cantor, M. Cárdenas-Barrantes, and L. F. Orozco, Pap. Phys. **14**, 140007 (2022).
[43] F. Dubois, V. Acary, and M. Jean, C. R. Mec. **346**, 247 (2018).
[44] M. Jean, Comput. Methods Appl. Mech. Eng. **177**, 235 (1999).
[45] M. Renouf, F. Dubois, and P. Alart, J. Comput. Appl. Math. **168**, 375 (2004).
[46] P. A. Cundall and O. D. L. Strack, Géotechnique **29**, 47 (1979).
[47] F. Radjai and F. Dubois, *Discrete-element Modeling of Granular Materials* (Wiley-Iste, London, UK, 2011).
[48] E. Azéma, N. Estrada, and F. Radjai, Phys. Rev. E **86**, 041301 (2012).
[49] A. Donev, R. Connelly, F. H. Stillinger, and S. Torquato, Phys. Rev. E **75**, 051304 (2007).
[50] J.-N. Roux, Phys. Rev. E **61**, 6802 (2000).